



# Li-Rich Layered Sulfide as Cathode Active Materials in All-Solid-State Li–Metal Batteries

Florencia Marchini, Sujoy Saha, Daniel Alves Dalla Corte, Jean Marie Tarascon

## ► To cite this version:

Florencia Marchini, Sujoy Saha, Daniel Alves Dalla Corte, Jean Marie Tarascon. Li-Rich Layered Sulfide as Cathode Active Materials in All-Solid-State Li–Metal Batteries. ACS Applied Materials & Interfaces, 2020, 12 (13), pp.15145-15154. 10.1021/acsami.9b22937 . hal-03313852

**HAL Id: hal-03313852**

**<https://hal.science/hal-03313852>**

Submitted on 4 Aug 2021

**HAL** is a multi-disciplinary open access archive for the deposit and dissemination of scientific research documents, whether they are published or not. The documents may come from teaching and research institutions in France or abroad, or from public or private research centers.

L'archive ouverte pluridisciplinaire **HAL**, est destinée au dépôt et à la diffusion de documents scientifiques de niveau recherche, publiés ou non, émanant des établissements d'enseignement et de recherche français ou étrangers, des laboratoires publics ou privés.

# A Li-rich layered sulfide as cathode active material in all-solid-state Li-metal batteries

*Florencia Marchini<sup>1</sup>, Sujoy Saha<sup>1,2,3</sup>, Daniel Alves Dalla Corte<sup>1</sup>, Jean Marie Tarascon<sup>1,2,3</sup> \**

<sup>1</sup>Collège de France, Chaire de Chimie du Solide et de l'Energie, UMR 8260, 11 Place Marcelin Berthelot, 75231 CEDEX 05 Paris, France

<sup>2</sup>Réseau sur le Stockage Electrochimique de l'Energie (RS2E), FR CNRS 3459, 33 Rue Saint Leu, 80039 Amiens, France

<sup>3</sup>Sorbonne Universités, 4 Place Jussieu, F-75005 Paris, France

\*e-mail: [jean-marie.tarascon@college-de-france.fr](mailto:jean-marie.tarascon@college-de-france.fr)

## ABSTRACT

Great hopes are placed on all-solid state Li-metal batteries (ASSB's) to boost the energy density of the current Li-ion technology. Though, these devices still present a number of unresolved issues that keep them far from commercialization such as interfacial instability, lithium dendrite formation and lack of mechanical integrity during cycling. To mitigate these limiting aspects, the most advanced ASSB systems presently combine a sulfide or oxide-based solid electrolyte (SE) with a coated Li-based oxide as positive electrode and a lithium anode. Through this work we propose a different twist by switching from layered oxides to layered sulfides as active cathode materials. Herein we present the performance of a Li-rich layered sulfide of formula  $\text{Li}_{1.13}\text{Ti}_{0.57}\text{Fe}_{0.3}\text{S}_2$  (LTFS) in room temperature operating all-solid state batteries, using  $\beta\text{-Li}_3\text{PS}_4$  as a solid electrolyte and both InLi and Li anode materials. These batteries exhibit good cyclability, small polarization and, in the case of Li anode, no irreversible capacity. Taking advantage of the stable LTFS/ $\beta\text{-Li}_3\text{PS}_4$  interface, we also propose the use of LTFS mixed with an

oxide-based cathode material in the positive electrode of an ASSB. Our proof of concept using  $\text{LiNi}_{0.6}\text{Mn}_{0.2}\text{Co}_{0.2}\text{O}_2$  (NMC 622) showed that the addition of a small amount of LTFS had a direct positive impact in the battery performance, ascribed to the improvement of the oxide cathode/sulfide SE interface.

## INTRODUCTION

Batteries are nowadays the most versatile and efficient mean of energy storage and play a key role in the energy transition from fossil fuels to renewable energies<sup>1</sup>. They have become essential for a wide range of strategic industries dealing with consumer electronics, electrical mobility and load levelling for grid management. Particularly, Li-ion batteries are presently the systems of choice for these applications. However, to sustain this leadership, research endeavours must target the ever-increasing specific-gravimetric energy density demands driven by electric vehicles. Overall, there are three main paths to achieve this goal. The first one is by feats of cell engineering, namely decreasing the amount of dead space and weight. The second is to develop new chemistries which would enable higher energy density electrodes, as exemplified by pioneering work on anionic redox<sup>2,3</sup>. Thirdly, intense research is presently directed towards the development of solid state batteries which, based on the use of Li-metal anode as well as adapting bipolar electrode stacking configuration, could outperform today's Li-ion cell performance<sup>4</sup>.

The concept of thin film solid-state batteries has been known for nearly 50 years<sup>5</sup>. However, due to the lack of highly conductive solid electrolytes (SE's), this research topic nearly falls into oblivion. It was rekindled back to 2011 with the discovery by Kanno's group of a new ionic conductor phase  $\text{Li}_{10}\text{GeP}_2\text{S}_{12}$  which conductivity equals that of today Li-ion liquid electrolyte ( $1.10^{-2}$  S/cm)<sup>6</sup>. Since then, solid-state batteries have become the source of worldwide excitement

evidenced by numerous industrial press releases and the colossal amount of research groups re-directing their work towards this topic. Yet, the excitement starts to be tarnished by the increasing awareness of the recurrent difficulties associated to interfaces and the use of Li-metal. Current research in ASSB's is parted between two approaches; both rely on a Li-metal negative electrode but differ in the nature of the solid electrolyte. This can be either a sulfide-based ionic conductor<sup>7,8</sup> (such as  $\text{Li}_3\text{PS}_4$ ,  $\text{Li}_7\text{Ge}_2\text{S}_{12}$  and  $\text{Li}_6\text{PS}_5\text{Cl}$ ) as well as an oxide ionic conductor pertaining to the garnet (LZZO) or perovskite (LTP) families<sup>9,10</sup>. The latter approach will not be considered here. Whatever the option pursued, several roadblocks remain prior to consider commercialization of ASSB's, as they still suffer interfacial instability, lack of mechanical integrity upon cycling and Li dendrite growth<sup>11-13</sup>.

Interfacial instabilities arise from the use of positive and negative electrodes having redox activities outside the stability window of the solid electrolytes. DFT calculations have shown that this window is usually narrower for ionic conducting sulfides (1-3 V for  $\beta\text{-Li}_3\text{PS}_4$ ) than for oxides (0- 4V for LZZO)<sup>14</sup>. To mitigate this in the anode side, most of today's sulfide electrolyte-based ASSB's take advantage of a Li-alloyed negative electrode for being less reductive than pure Li, as the case of the widely used In/InLi system<sup>15,16</sup>.

Turning to the positive electrode, the common choice falls on high voltage redox materials for preserving high energy densities, such as primarily layered, spinel, or olivine oxides presently used in liquid Li-ion technologies. However, the redox potential of these oxides far exceeds the thermodynamic stability of the ionic conducting sulfide<sup>17</sup>.

Additionally, the existing difference in the electrochemical potential of  $\text{Li}^+$  between the oxide cathode material and the sulfide solid electrolyte brings along, when put in contact, either a chemical reaction between them or the formation of a Li-depleted layer at the interface, which is

known as “space charge layer effect”<sup>18,19</sup>. This depleted layer is translated into a highly resistive cathode/SE interface, which is detrimental for the cell functioning for blocking the ion transport. To contour this problematic the current workable solution is to interpose a buffer layer between the cathode material and the solid electrolyte<sup>20</sup>. This layer is introduced as a thin surface-coating onto the cathode particles by means of different coating techniques. The approach of coating mimics the role of the SEI in Li-ion batteries, which is electronically insulators and Li<sup>+</sup> conductors<sup>21</sup>. Some examples of suitable coating materials meeting these requirements are LiNbO<sub>3</sub>, ZrO<sub>2</sub>, Li<sub>4</sub>Ti<sub>5</sub>O<sub>7</sub>, Al<sub>2</sub>O<sub>3</sub> and LiTaO<sub>3</sub>. Nevertheless, the need of coated cathode materials represents an additional step in the preparation of the positive electrode that can be both time consuming and very costly. In the search for alternative solutions to the interface issues in the positive electrode of ASSB’s, we come up with a different approach, which is the use of Li-active sulfides, either as active cathode materials or blended with Li-active oxide cathode materials.

Anionic redox chemistry has emerged as a new paradigm to design cathode materials with high energy density for lithium-ion batteries<sup>3</sup>. In the last decade, our group has built up a strong expertise in the solid state chemistry of both “practical” and “model” anionic redox compounds<sup>22–24</sup>. One of our most recent works concerns a novel high capacity Li-rich sulfide Li<sub>1.13</sub>Ti<sub>0.57</sub>Fe<sub>0.3</sub>S<sub>2</sub> (theoretical capacity 261 mAh/g, hereafter referred as LTFS), which presents both cationic and anionic redox activity involving Fe<sup>2+/3+</sup> and S<sup>2-/S<sup>n-</sup></sup> ( $n > 2$ ), respectively<sup>25</sup>. We have already carried out an in-depth study of the redox chemistry of LTFS in liquid cells. Herein we report its direct implementation in room temperature operating ASSB’s using different anode materials, including Li metal.

At a side of this work we also suggest the possibility of using this Li-rich sulfide mixed with oxide cathode materials as part of the positive electrode in ASSB's in order to improve the cathode/sulfide SE interface.

## EXPERIMENTAL

### Materials

*Li<sub>1.13</sub>Ti<sub>0.57</sub>Fe<sub>0.3</sub>S<sub>2</sub> (LTFS).* LTFS was prepared by ceramic synthesis. For this purpose, 259.6 mg of Li<sub>2</sub>S (Alfa Aesar, 99 wt. %), 728.4 mg of TiS<sub>2</sub> (Sigma Aldrich, 99.9 wt. %) and 263.7 mg of FeS (Alfa Aesar, 99 wt. %) were weighed and hand-grinded for 30 minutes. The precursor mixture was placed within a quartz tube in an Ar-filled glovebox (O<sub>2</sub> and H<sub>2</sub>O level < 1 ppm) which was further sealed under vacuum (~10<sup>-5</sup> mbar). The sealed tube was annealed at 750 °C for 36 h followed by quenching in water. The resulting compound was collected inside a glovebox and hand-grinded for 10 minutes.

*Solid electrolyte.* The nanoporous β-Li<sub>3</sub>PS<sub>4</sub> solid electrolyte was obtained from Li<sub>2</sub>S (Alfa Aesar, 99 wt. %) and P<sub>2</sub>S<sub>5</sub> (Acros Organics, purity > 98 wt. %) via solution synthesis in tetrahydrofuran (THF) described elsewhere<sup>26</sup>. The ionic conductivity of the resulting powder determined by EIS was 0.16 mS/cm (figure S1b) while the crystal structure was corroborated by XRD (figure S1c).

*Composite preparation for chemical compatibility tests.* Within an argon-filled glove box the corresponding compounds (LTFS, β-Li<sub>3</sub>PS<sub>4</sub> or NMC 622) were first weighted in the desired ratio and then mixed by hand grinding with a mortar and pestle for 30 minutes. Around 100 mg to 200

mg of the mixture were placed into a dye set and compressed applying 4 tons/cm<sup>2</sup> with an hydraulic press during 5 minutes to form a pellet of 8mm diameter. The thickness was measured in each case to determine the conductivity. The pellet was later removed from the dye set and placed into the electrochemical testing cell where the heating treatment and DC conductivity measurements were performed.

### **Characterization**

*Thermogravimetric analysis (TGA).* In order to evaluate the air stability of LTFS, TGA was conducted using a Mettler Toledo TGA/DSC 3+ (LF1100 °C) equipment. The measurement was performed during 24 hours, in isothermal conditions (25°C) and under constant flow of dry synthetic air. The initial mass of sample was 33.72 mg.

*S-XRD and XRD.* Synchrotron X-ray powder diffraction (SXRD) patterns collected at the MSPD beamline of the ALBA synchrotron facilities (Barcelona, Spain). All SXRD data were collected in transmission mode with  $\lambda = 0.4418 \text{ \AA}$ , with the powder sealed in a quartz capillary of diameter 0.7 mm. Laboratory X-ray powder diffraction (XRD) were performed in an airtight cell equipped with a Be window. XRD patterns were recorded in reflection mode in Bragg–Brentano geometry using a Bruker D8 Advance diffractometer equipped with a Cu-K $\alpha$  X-ray source ( $\lambda_1 = 1.54056 \text{ \AA}$ ,  $\lambda_2 = 1.54439 \text{ \AA}$ ) and a LynxEye detector. The refinements of the patterns were done using the Rietveld method as implemented in the FullProf program.

*Scanning electron microscopy.* Cross-sectional and top-view micrographs of full cells and pristine compounds were obtained on a high-resolution scanning electron microscope (Oxford

Instruments). The cross sections were obtained within the Ar-filled glovebox by carefully cutting the pellets previously embedded in conductive epoxy. Energy-dispersive X-ray spectroscopy (EDS) of the composite cathode was carried out using an acceleration voltage of 20 kV.

### **Battery assembling and electrochemical testing**

The electrochemical testing of ASSB's (which comprised battery cycling, electrochemical impedance spectroscopy and chronoamperometry) was performed in a cell fully designed in our laboratory (figure S2). The cell can be described as the assembly of three cylinder-shaped separated elements, these being an upper and lower stainless steel piston (8 mm diameter) and a central body part. Both the pistons and the central body are insulated with an outer case of polyethylenimine (PEI). For the cell operation, the two pistons are inserted within a 8 mm diameter PEI sleeve in the central piece and further placed in an stainless steel frame (not shown). The pressure required for cycling is applied uniaxially onto the upper piston by means of an upper screw passing through the frame. The middle part of the cell is also equipped with a heating system enabling different temperature regimes up to 200°C. Moreover, the system also counts with a pressure sensor for pressure control and monitoring.

The solid state batteries were assembled within the aforementioned cell by sequential loading and cold pressing of each component, these being 1- the solid electrolyte, 2- the cathode composite, 3- the metallic foil (In and/or Li) and 4- the Cu current collector.

The cathode composite in all cases consisted in a mixture of the active cathode material (LTFS or LTFS+NMC 622, respectively) with the solid electrolyte  $\beta$ -Li<sub>3</sub>PS<sub>4</sub> in a 70:30 wt. %. The composite was prepared by hand grinding the powders with a mortar and pestle for 1 hour.



For the battery assembling 30-35 mg of solid electrolyte are firstly loaded in the cell and homogeneously distributed within the middle sleeve and onto the lower piston. The cell is then closed and a pressure of  $0.2 \text{ ton/cm}^2$  is applied for 1 minute by means of an hydraulic press. Next, the upper piston of the cell is removed and 5-10 mg of the cathode composite are loaded and homogeneously spread onto the surface of the pre-compressed solid electrolyte layer. The cell is closed again and pressed up to  $4 \text{ ton/cm}^2$  during 5 minutes. Next, the lower piston is removed from the cell and the metallic anode previously spread onto a 8 mm diameter Cu disk is introduced within the sleeve in the middle part of the cell facing the solid electrolyte layer. Depending on the case, the metallic anode was either an InLi alloy or metallic Li. For the first case, 0.5 mg of Li and 20 mg of In were spread onto the Cu disk forming a biphasic system of approximate molar ratio  $0.4 \text{ InLi} / 0.6 \text{ In}$ . For preparing Li metal anodes, a piece of Li foil between 1mg to 3 mg was spread to fully cover the Cu current collector. The cell is finally closed and positioned in a stainless steel frame with a screw on top, which provides the pressure needed for cycling by pressing, when screwed, the upper piston of the cell. The pressure set for cycling was in all cases  $0.7 \text{ ton/cm}^2$ .

Galvanostatic cycling of the cells was carried out in the voltage range of 1.2–2.4 V vs InLi/Li<sup>+</sup> or 1.8–3.0 V vs Li/Li<sup>+</sup> in the case of LTFS and 2.1-3.7 V vs InLi/Li<sup>+</sup> in the case of NMC 622 .

Electrochemical impedance spectroscopy (EIS) was performed onto the full batteries, in discharged or charged state as indicated. An excitation amplitude of 50 mV was applied in the indicated frequency range with 15 points per decade.

Chronoamperometry was used to determine the electronic conductivity (hereafter referred as DC conductivity) of the pelletized composites. For this purpose, subsequent potential steps were applied to each sample while recording the current until it reached a stationary value. The potential applied and the time of measurement were adjusted depending on the nature and dimensions of each pellet. The DC conductivity was obtained using the formula  $\sigma_{DC} = \frac{l}{A \cdot R}$ , in which  $l$  and  $A$  are the thickness and the surface area of the pellet, respectively, and  $R$  is the reciprocal of the slope in the  $i_{stationary}$  vs  $E_{applied}$  plot.

All the electrochemical tests were conducted using the VMP3 electrochemical workstation by Bio-Logic Science Instruments SAS.

## RESULTS AND DISCUSSION

Figure 1 recaps the synchrotron X-ray diffraction (SXRD) pattern and the SEM micrographs of the as-synthesized  $Li_{1.13}Ti_{0.57}Fe_{0.3}S_2$  powder. The micrographs revealed monolithic pseudo spherical particles of sizes ranging from 5  $\mu m$  to 20  $\mu m$  (figures 1a, 1b).

FIGURE 1 HERE

The SXRD pattern (figure 1c) confirmed the presence of a single crystalline phase with no observable residual impurities. According to Rietveld refinement, LTFS crystal structure can be described as an hexagonal phase ( $R\bar{3}m$  space group) with lattice parameters  $a=3.53 \text{ \AA}$  and  $c=18.09 \text{ \AA}$ . This structure is analogous to the well-known layered Li-rich  $Li_{1+y}M_{1-y}O_2$  phases, but

with a larger unit cell to accommodate the bulkier  $S^{2-}$  ligands. Notice that the structure is cation ordered, with Fe atoms located in the same sites as Ti/Li within the metal layer (figure 1d).

LTFS was characterized for its air-moisture stability and its chemical stability against the solid electrolyte. XRD coupled with isothermal thermo-gravimetric analysis performed at 25°C reveals that this compound is moisture sensitive in a non-controlled moisture environment but air resistant, making it feasible to handle it in a dry room. (figure S3).

Lastly, the compatibility between LTFS and the solid electrolyte  $\beta$ -Li<sub>3</sub>PS<sub>4</sub> was checked through XRD and DC conductivity measurements on a LTFS/ $\beta$ -Li<sub>3</sub>PS<sub>4</sub> (70/30 wt. %) composite before and after a heating treatment at 200°C for 5 days. The heating was herein used to promote decomposition reactions and it was performed in-situ within the electrochemical testing cell. Rietveld refinement of the XRD data confirmed the presence of only LTFS and  $\beta$ -Li<sub>3</sub>PS<sub>4</sub> in the heated composite with no extra peaks (figure 1e). On the other hand, the electrical conductivity was also found to remain constant after the thermal treatment, being approximately  $5 \cdot 10^{-3}$  S/cm (figure 1f). In contrast, analogous experiments performed on a pelletized NMC 622/ $\beta$ -Li<sub>3</sub>PS<sub>4</sub> composite (70/30 wt. %, NMC 622 d<sub>50</sub>: 12  $\mu$ m) showed visible changes in the XRD pattern and a drop of the DC conductivity from 0.0210 mS/cm to 0.0035 mS/cm after the thermal treatment, hinting on the presence of interphases of decomposition products (figures S4 a, b).

In short, these results highlight the chemical stability towards the solid electrolyte exhibited by LTFS unlike the observed for NMC 622. This was somehow expected, based on the higher stability of the sulfide/sulfide interface compared to the sulfide/oxide interface and well explains why no buffer interlayer is needed for LTFS. Moreover and of great importance for battery assembling is the remarkably high electronic conductivity of the LTFS/ $\beta$ -Li<sub>3</sub>PS<sub>4</sub> composite. This

is ascribed to the large electronic conductivity of pristine LTFS (20 mS/cm) and makes unnecessary the addition of any conductive agent.

### **LTFS || InLi all-solid state battery**

In order to test LTFS performance as cathode material in ASSB's and based on previous literature work, the InLi alloy was our anode of first choice. Such an alloy is less reductive than pure Li (0.6 V vs. Li/Li<sup>+</sup>) and therefore provides better interface stability.

FIGURE 2 HERE

**Figure 2a** exhibits the SEM micrograph and the EDS mapping of the cross sectional view of a fresh assembled **LTFS+ $\beta$ -Li<sub>3</sub>PS<sub>4</sub> (70-30 wt. %)| $\beta$ -Li<sub>3</sub>PS<sub>4</sub>|InLi** full battery. Three dense layers can be distinguished corresponding, from bottom to top, to the InLi anode, the  $\beta$ -Li<sub>3</sub>PS<sub>4</sub> solid electrolyte and the LTFS+ $\beta$ -Li<sub>3</sub>PS<sub>4</sub> cathode composite. The porosity of each layer estimated according to its mass, area and average thickness, was found to equal ~10% for the SE layer ( $\beta$ -Li<sub>3</sub>PS<sub>4</sub> bulk density: 1.85 g/cm<sup>3</sup>)<sup>27</sup> and ~23% for the cathode composite (weighted average density of the composite: 2.61 g/cm<sup>3</sup>, LTFS bulk density: 2.94 g/cm<sup>3</sup>). The good densification of the solid electrolyte can be attributed to its low Young's Modulus (29.5 GPa)<sup>28</sup> which reflects the characteristic softness of sulfides<sup>29</sup>. A smooth cross-section transition when going from the positive electrode to the SE is also observed, showing a good contact between layers. Moreover, the even distribution of Ti and P in cathode layer evidences an homogeneous LTFS/ $\beta$ -Li<sub>3</sub>PS<sub>4</sub> composite, while keeping electronic percolation. Regarding the anode side, it exhibits a rather

homogeneous thickness of around 80  $\mu\text{m}$  with a region of contact loss at the edge most likely inflicted during the cutting of the pellet.

**Figure 2b** depicts the galvanostatic charge/discharge voltage profiles together with the discharge capacity and coulombic efficiency (**figure 2c**) for the ASSB **LTFS+ $\beta$ -Li<sub>3</sub>PS<sub>4</sub>(70-30 wt. %)| $\beta$ -Li<sub>3</sub>PS<sub>4</sub>|InLi** at C/25 and different temperatures. The voltage trace exhibits a long plateau-like redox activity at 2.1 V (2.7 V in the Li/Li<sup>+</sup> scale) during the first charge, in line with the reported first formation cycle for this material in a liquid electrolyte half-cell (LP30, Li metal anode)<sup>25</sup>. This activation cycle is then followed by subsequent cycles at lower voltage with profiles of similar shape, good reversibility and capacity retention.

The polarization during cycling, determined as  $E_{\text{charge}} - E_{\text{discharge}}$  at 120 mAh/g, is indicated in the figure with a dashed line and expectedly decreases with temperature, due to improved kinetics. A significant capacity loss was observed during the 1<sup>st</sup> cycle (69% of coulombic efficiency, 50 mAh/g of irreversible capacity). From the 2<sup>nd</sup> cycle on, a reversible capacity of 120 mAh/g was obtained at room temperature and further raised to 140 mAh/g at 100°C. However, this still represents only the 54% of the reversible capacity obtained at C/20 in the liquid half-cell. The latter, despite disappointing, is in line with existing research repeatedly showing that the reversible capacity delivered by a given cathode material in an ASSB configuration is always lower than in an analogous liquid cell. This effect can be explained in terms of ion transport, as liquid electrolytes provide a better wettability of the active material and a greater ionic conductivity than solid electrolytes ( $\sigma_{\text{ion}}$  for LP30 is 50 times larger than for  $\beta$ -Li<sub>3</sub>PS<sub>4</sub>)<sup>30</sup>.

To minimize the mass transport limitations another ASSB was cycled at room temperature but at a lower C-rate (C/50). In these conditions (**figure 3**), the reversible capacity expectedly raised from 120 mAh/g to 145 mAh/g while the overpotential decreased from 206 mV to 155 mV. Note

equally, that the cell showed 90% of capacity retention after 10 cycles with an irreversible capacity loss after the first cycle of 27% solely as compared to 46% previously.

FIGURE 3 HERE

The electrochemical stability of the positive electrode upon cycling was firstly evaluated at the crystal structure level. Rietveld refinement of the S-XRD pattern corresponding to the discharged cathode composite showed neither structural changes for LTFS or  $\beta$ -Li<sub>3</sub>PS<sub>4</sub> nor appearance of new phases after the first cycle of the battery (figure S5, RIGHT)

For assessing stability at the cathode/SE interface level, EIS of the full cell of figure 2 was measured in the pristine and discharged state after 1<sup>st</sup>, 2<sup>nd</sup> and 3<sup>rd</sup> cycle. The corresponding Nyquist plots are shown together in figure 4. The interpretation the EIS data was done following the model suggested by Tatsumisago et. al. and Zhang et.al. According to this model, the high frequency range of the spectra (HF, ~ 0.5 MHz - 10 kHz) is been ascribed to the solid electrolyte resistance, whereas the middle frequency (MF, ~10 kHz – 10 Hz) and low frequency (LF, ~10 Hz – 10 mHz) ranges are assigned to the contribution of the cathode/solid electrolyte and anode/solid electrolyte interfaces, respectively<sup>31,32</sup>. Since this work focuses in the cathode material, we limited our analysis to the HF-MF region.

The HF region our spectra (>30 kHz) was fitted with one RQ element (defined as a parallel R-CPE connection) which univocally corresponds to the resistance of the SE ( $R_{Q_{HF}}$ ,  $C_{HF}$ ~ 50 nF). As for the MF part of the spectra (30 KHz-1kHz) one RQ element was also required ( $R_{Q_{MF}}$ ,  $C_{MF}$ ~ 10  $\mu$ F) and assigned to the CM/SE interface resistance.

FIGURE 4 HERE

Except in the pristine battery where no  $R_{Q_{MF}}$  component could be fitted, the CM/SE interface resistance was in all cases between 50-70  $\Omega$ . These are very small resistance values and comparable to the reported for different coated oxide cathode/sulfide solid electrolyte interfaces<sup>32</sup>. We can therefore affirm that LTFS provides a low resistive interface with the solid electrolyte without the need of any buffer layer. This is consistent with the fact that both are S-based compounds and no formation of space charge layer is expected and with the lower operational voltage of LTFS compared to oxides. Consequently, low voltage/high capacity cathode materials may come up as one strategy to mitigate CM/SE interface issues without sacrificing energy density. Moreover, these results rule out interfacial reactions involving LTFS as the source of the irreversibility observed in the first cycle.

On the other hand, the calculated SE resistance in the freshly assembled battery was found to be 529  $\Omega$  (in good agreement with the conductivity determined for the pristine  $\beta$ -LPS) which then increases to 640-670  $\Omega$  after cycling. This might be an indication of electro-mechanical degradation of the pellet probably related to the huge volume changes of the InLi anode upon cycling (~53%).

### **LTFS || Li all-solid state battery**

We have mentioned that one of the major advantages of ASSB's over the current Li-ion technology relies in the boost of the energy density. In this context, lithium-alloyed negative electrodes are impractical as they provide lower cell voltage (compared to Li) and the alloying metals are heavy and often very costly (as in the case of Indium). Thus, together with the

obvious gain when using Li-metal anodes, the old unresolved problems of reactivity and dendrite growth re-emerge. However, encouraged by the promising performance found for LTFS in ASSB's, we moved one step forward towards a practical all-solid state system by introducing a Li metal anode.

An all solid state LTFS+ $\beta$ -Li<sub>3</sub>PS<sub>4</sub>(70-30 wt. %)| $\beta$ -Li<sub>3</sub>PS<sub>4</sub>|Li battery was assembled **Figure 5a**. Its cross sectional view shows a dense and continuous stack with no visible cracks together with good contact between the layers. Moreover, porosity values regarding positive electrode and electrolyte were found to be similar to the ones estimated for the LTFS||InLi battery. The cell voltage profiles for the 1<sup>st</sup> and 10<sup>th</sup> galvanostatic charge/discharge cycles are shown **in figure 5b**. **In figure 5c** the evolution of the discharge capacity and coulombic efficiency along the first 10 cycles are also shown. Note that low cycling rate (C/50) was used here to prevent dendrites growth.

FIGURE 5 HERE

The voltage capacity traces exhibit low polarization (85 mV determined at 120 mAh/g) with no capacity loss and coulombic efficiencies above 99%. A reversible capacity of 214 mAh/g after 10 cycles was obtained, which represents the 83 % of the theoretical capacity and corresponds to the removal of 0.94 Li per LTFS unit formula. These are striking numbers for intercalation chemistries in room temperature operating ASSB's. To our knowledge, the reversible capacity of lithiated oxide-based cathode materials never surpasses the 140 mAh/g, even with conductive additives<sup>31,33</sup>. When it comes to sulfide-based intercalation compounds, only disordered Li<sub>2</sub>TiS<sub>3</sub> has been reported to deliver 275 mAh/g after 10 cycles with 91% of retention in a carbon-containing ASSB operating at 50°C.<sup>34</sup>



## FIGURE 6 HERE

To get a better insight of the interface phenomena upon cycling, EIS was performed on the same cell as above in the discharged state after the 6<sup>th</sup> and the 10<sup>th</sup> cycle. The corresponding Nyquist plots are shown in figure 6. The data was fitted with two series (RQ) elements and one constant phase element (Q) for the low frequency region. The resistance determined for the solid electrolyte was in both cases  $\sim 440\ \Omega$ , while the CM/SE interface resistance was found to be  $68\ \Omega$  and  $77\ \Omega$  for the 6<sup>th</sup> and 10<sup>th</sup> cycle, respectively. As it was previously discussed for the LTFS || InLi system, these values are also in line with a nearly resistive-free CM/SE interface. The small difference between them also gives an account on the stability of the interface, even at very low C-rate when parasitic reactions are usually magnified.

Based on the absence of new processes in the LF region, this battery does not seem to present SE stability issues towards the Li anode either. However, Li anodes have other intrinsic problem that calls for solution: dendrite growth. In ASSB's, inhomogeneous current densities give rise to nucleation of dendrites in the electrode surface and in the SE grain boundaries limiting the rate capability<sup>12,35</sup>. For this reason we were obliged to cycle at C/50, as faster C-rates eventually led to short circuiting of the cell.

As it stands out, the LTFS||Li battery presented no irreversibility during the first cycle, less than half of polarization and better capacity retention than the previously shown LTFS||InLi.

Furthermore, no SE resistance increase and negligible evolution of the CM/SE interface was evidence by EIS. Logically, these discrepancies seem to point towards the nature of the negative electrode. Whereas it is not in the scope of this work to perform a comparative study on anode

materials for ASSB's, our observations lead to question the reliability of the widely used InLi alloy as a model anode for cathode testing.

### **LTFS as NMC/ $\beta$ -Li<sub>3</sub>PS<sub>4</sub> buffer layer**

We have heretofore shown LTFS performance in ASSB's as the Li-active cathode material. We have pointed out that a positive attribute of this compound relies on its high stability upon cycling, even at the interface level. At this stage, a legitimate question regards the possibility to use LTFS as the protective coating of a Li-insertion oxide electrode, hence replacing the electrochemically dead coatings (LiNbO<sub>3</sub>, Al<sub>2</sub>O<sub>3</sub>) so far used while serving as active buffer to decrease the NMC/ $\beta$ -Li<sub>3</sub>PS<sub>4</sub> interface resistance. Thus, we embarked in checking such an idea.

NMC 622 (particle size: d<sub>50</sub> 12 $\mu$ m) was first selected as the Li-active oxide to be mixed with LTFS. The chemical compatibility between LTFS and NMC 622 was firstly verified onto a pelletized NMC 622/LTFS (1:1 wt. %) composite following the same procedure previously described for the LTFS/ $\beta$ -Li<sub>3</sub>PS<sub>4</sub> mixture. (figure S6)

As a proof of concept of our approach, two all-solid state batteries (named as *Proof A* and *Proof B*) were assembled, with the first one being LTFS-free and the latter containing 7 wt. % of LTFS in the positive electrode.

*Proof A*: NMC 622:  $\beta$ -Li<sub>3</sub>PS<sub>4</sub> (70:30 wt. %)| $\beta$ -Li<sub>3</sub>PS<sub>4</sub>|InLi

*Proof B*: NMC 622: LTFS: $\beta$ -Li<sub>3</sub>PS<sub>4</sub> (63:7:30 wt. %)| $\beta$ -Li<sub>3</sub>PS<sub>4</sub>|InLi

*Proof A* and *Proof B* were galvanostatically charged/discharged at room temperature, at a cycling rate of C/50 and within a voltage window of 2.1-3.7 V vs InLi/Li<sup>+</sup> (2.7 V - 4.3 V in the Li/Li<sup>+</sup> scale).

The first galvanostatic charge/discharge cycle of both batteries are presented in Figure 6, together with the discharge capacity delivered along 10 cycles. Whereas *Proof A* exhibited the typical voltage profile of NMC 622 observed in ASSB's, *Proof B* presents an additional feature from 2.0 V to 2.15 V indicated in the graph with a dashed line and ascribed to the delithiation of LTFS. The results in figure 7 clearly show an improved performance for the battery containing LTFS respect to the one with solely NMC 622 in terms of reversible capacity and overvoltage. These results are in line with the lower resistance of the cathode/SE interface (determined from the MF region in the EIS spectra, figure S7) for *Proof B* (710  $\Omega$ ) compared to *Proof A* (1240  $\Omega$ ). Additionally, DC conductivity measurements performed onto the cathode composites of both *Proof A* and *Proof B* provide strong evidence that LTFS may also act as a conductive agent in the positive electrode. Even using LTFS of particle size far from optimal, the addition of 7% of LTFS boosted the electronic conductivity of the cathode composite from  $2.1 \cdot 10^{-5}$  S/cm to  $5.3 \cdot 10^{-5}$  S/cm (figure S4, c).

FIGURE 7 HERE

Despite being a mere proof of concept in which many parameters of importance have not been optimized (particles sizes, electrode composition, mixing technique, etc.)<sup>36,37</sup>, the results are truly promising. The addition of LTFS had a clear positive impact in the battery performance mainly ascribed to a lower CM/SE interface resistance. This brings sulfide-based coatings into consideration as an alternative cathode coating approach to mitigate the space-charge layer effect and parasitic reactions between oxide-based cathodes and sulfide-based solid electrolytes.

## CONCLUSIONS

In the present work we have reported  $\text{Li}_{1.13}\text{Ti}_{0.57}\text{Fe}_{0.3}\text{S}_2$  (LTFS) as a promising cathode material for all-solid state batteries. We firstly addressed chemical aspects and found this compound to be moisture sensitive but air resistant and chemical inert towards  $\beta\text{-Li}_3\text{PS}_4$  solid electrolyte. When testing its performance in model and practical ASSB's using InLi and Li anodes, respectively, LTFS exhibits good cyclability and capacity retention. In particular, good CM/SE interface stability was evidenced in both cases by EIS measurements. Moreover, a stunning performance was obtained when cycling LTFS against Li in terms of reversible capacity and polarization; all at room temperature and without the need of any coating or conductive agent. Conversely, significant capacity loss during the first cycle was observed when using an InLi anode leading us to question the reliability of the InLi alloy as a model anode material in ASSB's.

Finally, we found an improved battery performance when adding LTFS to an NMC-based all-solid positive electrode. We ascribed that improvement to the less resistive CM/SE interface evidenced by EIS. With this, we propose the use of Li-active sulfides as alternative coating compounds for oxide-based cathode materials in ASSB's. In a wider range, this work also aims to raise the awareness of the battery community that outside the universe of the high voltage oxide-based cathode chemistries there is a world of attractive possibilities yet to be explored and more so as we will be pursuing the uses of sulphides ionic conducting electrolytes.

## FIGURES

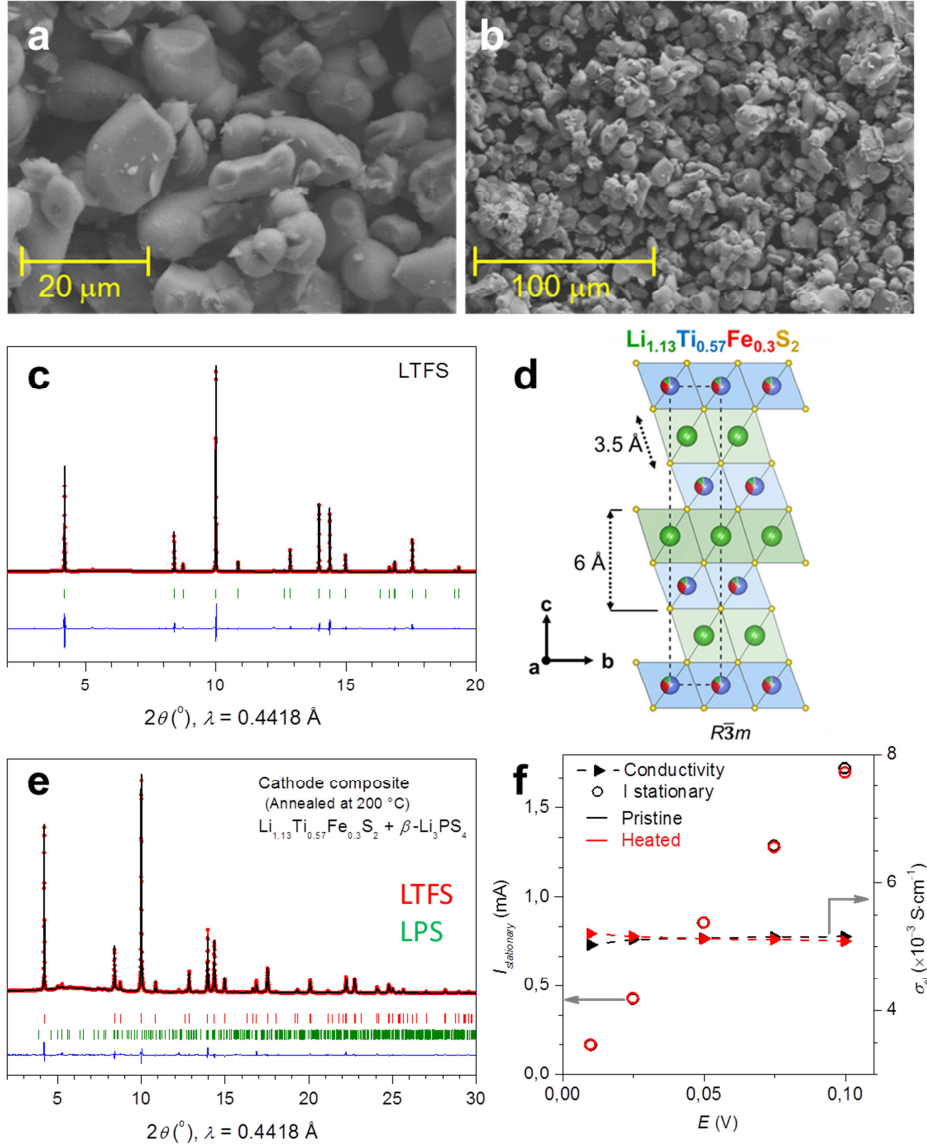


**Figure 1.** (a), (b) SEM micrographs of pristine  $\text{Li}_{1.13}\text{Ti}_{0.57}\text{Fe}_{0.3}\text{S}_2$  (LTFS) particles. (c) S-XRD pattern and Rietveld refinement of pristine LTFS. The red circles, black continuous line, blue line, and green tick bars represent the observed, calculated, and difference patterns, and Bragg positions, respectively. The S-XRD pattern was refined in  $R\bar{3}m$  space group with unit cell parameters  $a = b = 3.53166(1) \text{ \AA}$ ,  $c = 18.07285(9) \text{ \AA}$ ,  $V = 195.216(1) \text{ \AA}^3$  (d) Crystal structure of

LTFS. (e) S-XRD and Rietveld refinement of the LTFS/ $\beta$ - $\text{Li}_3\text{PS}_4$  (70-30 wt.%) composite after heating treatment at 200°C for 5 days. The SXRD pattern was refined in  $R\bar{3}m$  space group with unit cell parameters  $a = b = 3.53393(1) \text{ \AA}$ ,  $c = 18.06313(9) \text{ \AA}$ ,  $V = 195.362(1) \text{ \AA}^3$  (f) Stationary current (circles) and DC conductivity determination (triangles) measured on a pelletized LTFS/ $\beta$ - $\text{Li}_3\text{PS}_4$  (70-30 wt.%) composite before (black) and after (red) the heating treatment.

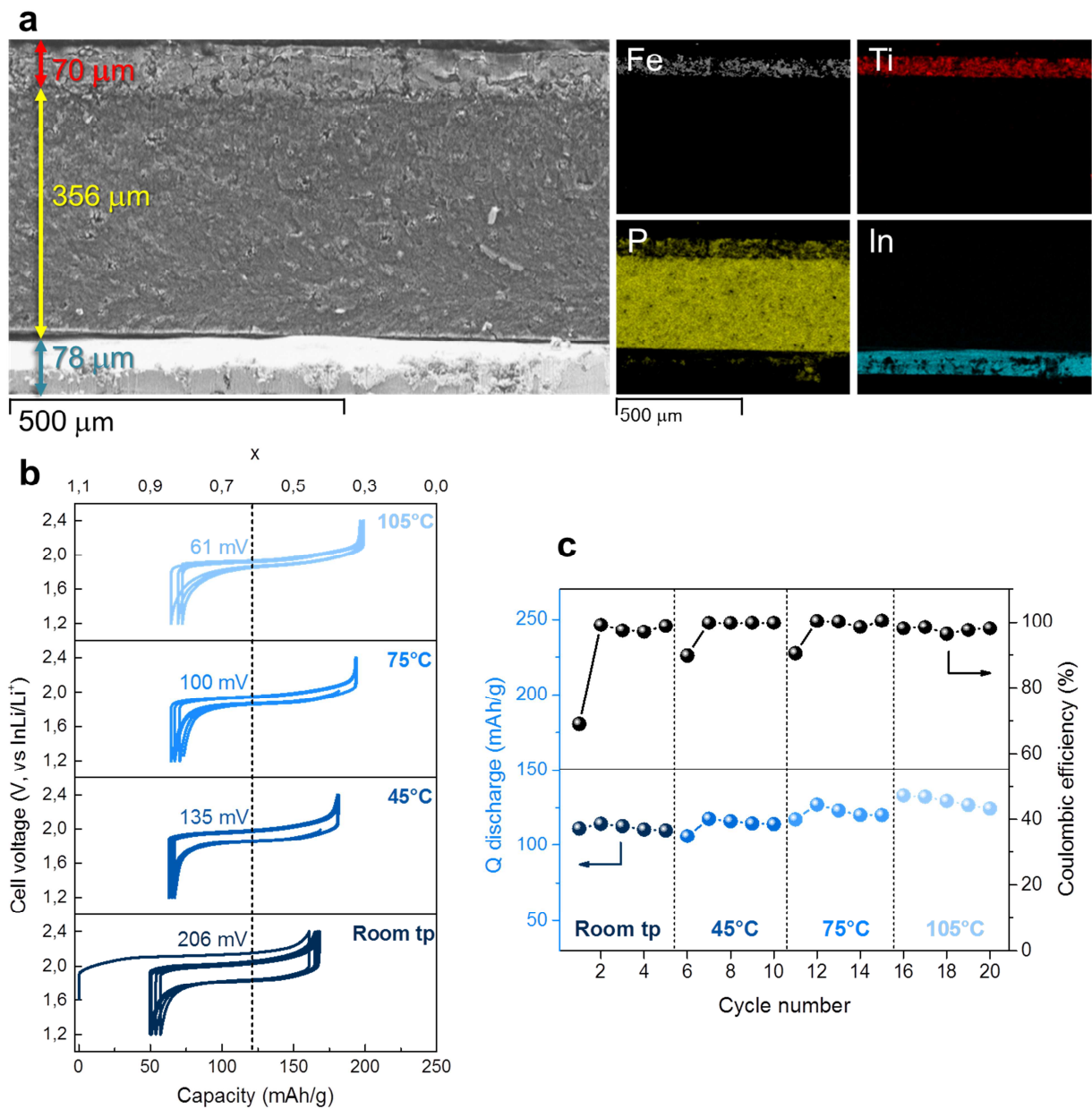


**Figure 2.** LTFS+ $\beta$ -Li<sub>3</sub>PS<sub>4</sub> (70-30 wt. %)| $\beta$ -Li<sub>3</sub>PS<sub>4</sub>|InLi battery. (a) SEM micrograph (LEFT) and EDS mapping (RIGHT) of the cross sectional view of the as prepared cell. (b) Galvanostatic charge/discharge curves, (c) discharge capacity and coulombic efficiency obtained at C/25 and different temperature regimes.

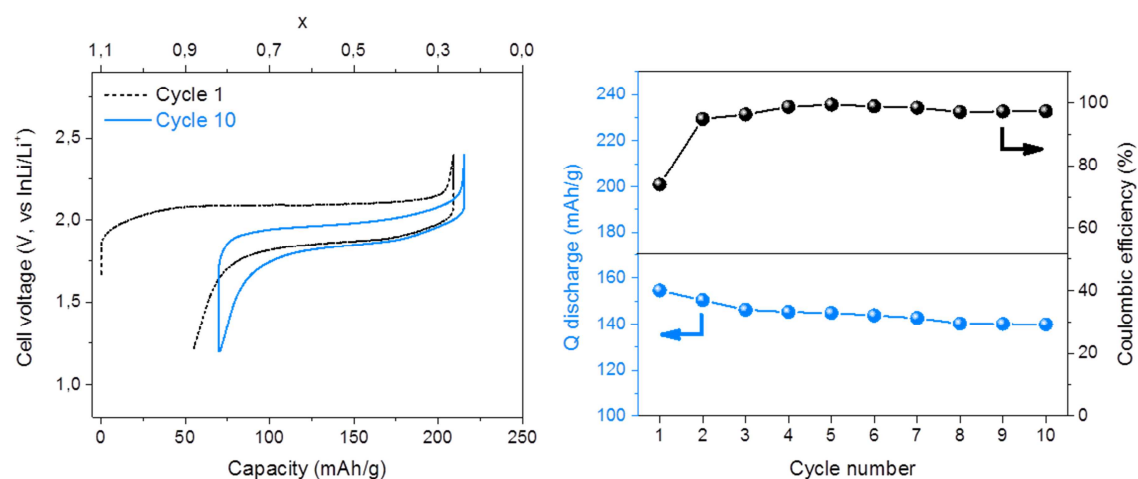


**Figure 3.** 1<sup>st</sup> and 10<sup>th</sup> galvanostatic charge/discharge cycles (LEFT), discharge capacity and coulombic efficiency (RIGHT) for the LTFS+ $\beta$ -Li<sub>3</sub>PS<sub>4</sub> (70-30 wt%)| $\beta$ -Li<sub>3</sub>PS<sub>4</sub>|InLi battery cycled at C/50 and at room temperature.

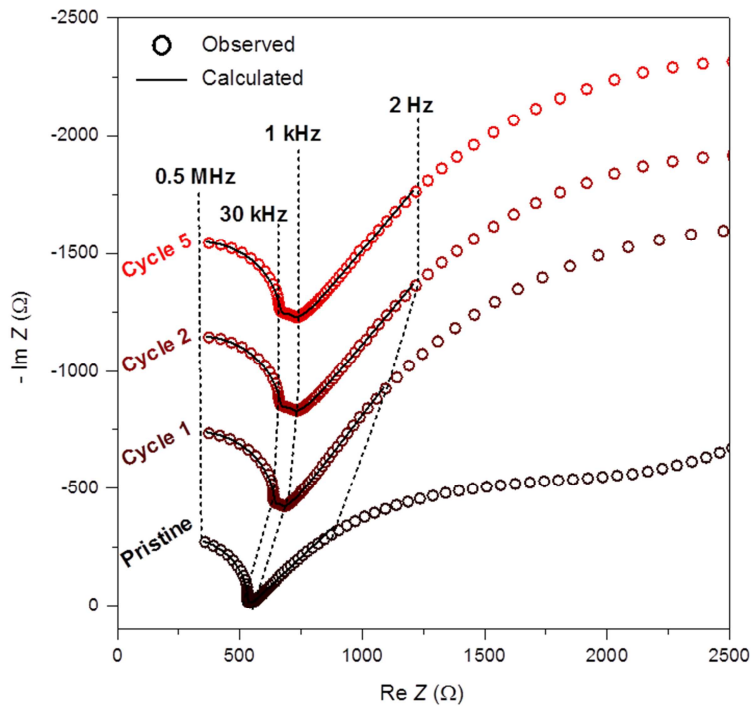


**Figure 4.** Nyquist plots from EIS measurements performed on the LTFS+ $\beta$ -Li<sub>3</sub>PS<sub>4</sub> (70-30 wt. %)| $\beta$ -Li<sub>3</sub>PS<sub>4</sub>|InLi battery presented in figure 2. The different curves correspond to the pristine battery after assembling and the discharged battery after the 1st, 2nd and 5th cycle. The measurements were performed after a resting period of 20h and in a frequency range 500 kHz – 10 mHz. Experimental data was further fitted between 0.5 MHz - 2 Hz with a (RQ)(RQ)Q equivalent circuit. For the stacking of the spectra a constant shift of -400  $\Omega$  in the Y axis was applied.



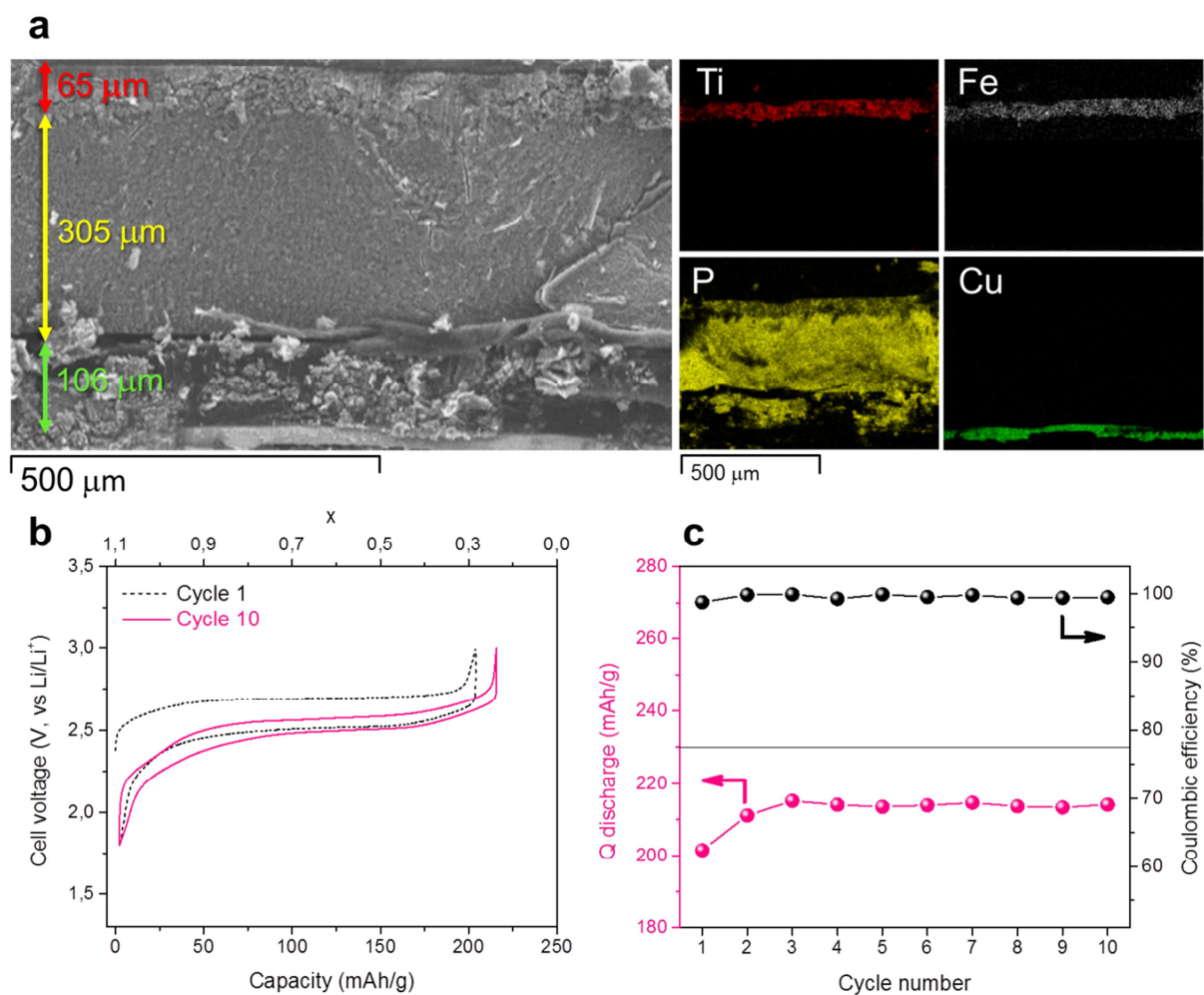


**Figure 5.** LTFS+ $\beta$ - $\text{Li}_3\text{PS}_4$  (70-30 wt. %)| $\beta$ - $\text{Li}_3\text{PS}_4$ |Li battery. (a) SEM micrograph (LEFT) and EDS mapping (RIGHT) of the cross sectional view of the as prepared battery (Since Li atoms cannot be detected in the EDS analysis, the Cu current collector was included to locate the anode) (b) 1<sup>st</sup> and 10<sup>th</sup> galvanostatic charge/discharge cycles, (c) discharge capacity and coulombic efficiency obtained at C/50 and room temperature. The presence of solid electrolyte partially covering the anode as well as the roughness of the electrolyte layer is due to the complexity of properly cutting the pellet.

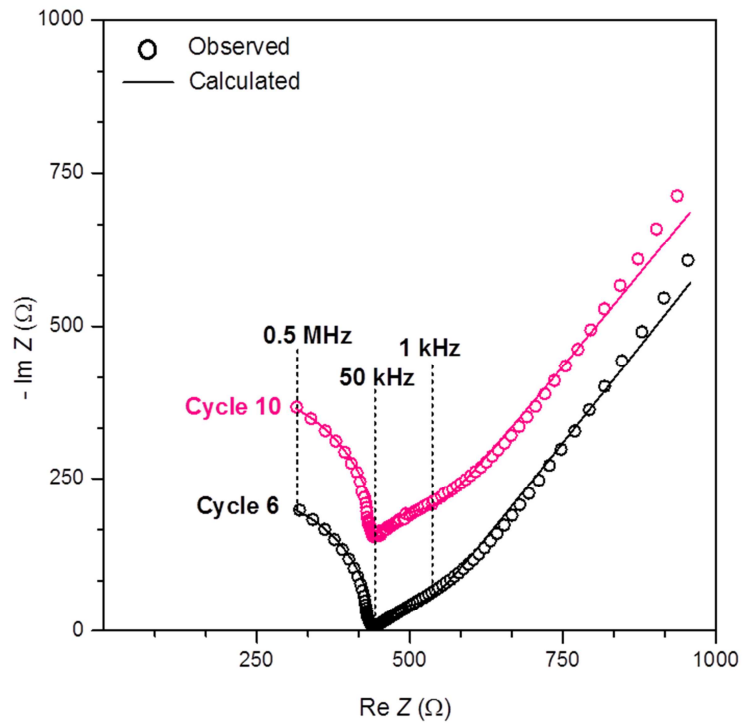


**Figure 6.** Nyquist plots from EIS measurements performed on the discharged LTFS+ $\beta$ - $\text{Li}_3\text{PS}_4$  (70-30 wt. %)| $\beta$ - $\text{Li}_3\text{PS}_4$ |Li battery presented in figure 5 after the 1<sup>st</sup> and 5<sup>th</sup> cycle. The measurements were performed after a resting period of 20h and in a frequency range 500 kHz – 10 mHz. Experimental data was fitted with a (RQ)(RQ)Q equivalent circuit. The spectrum of cycle 10 was intentionally shifted -150  $\Omega$  in the Y axis for clearer plotting.

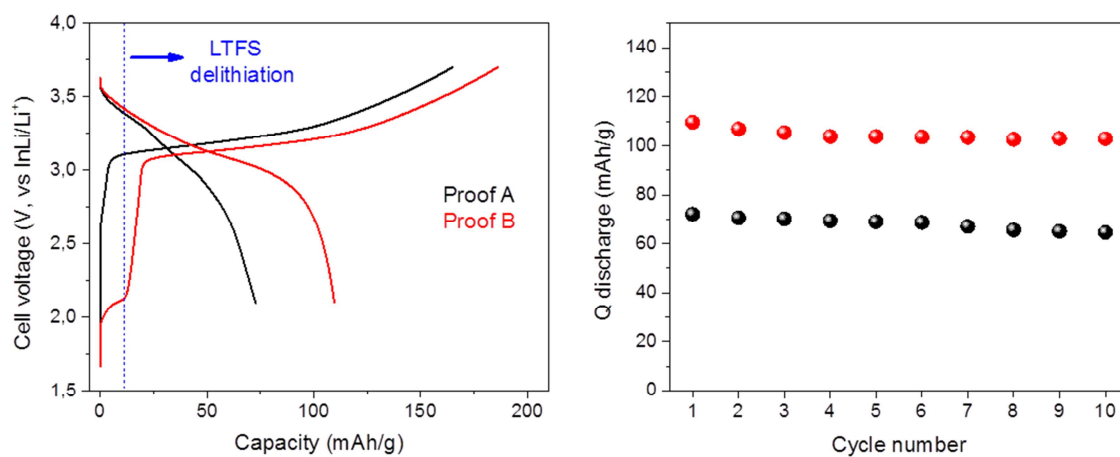


**Figure 7.** 1<sup>st</sup> galvanostatic charge/discharge cycle (LEFT), discharge capacity and coulombic efficiency (RIGHT) for Proof Battery A (black) and Proof Battery B (red) cycled at C/50 and room temperature.

## SUPPORTING INFORMATION

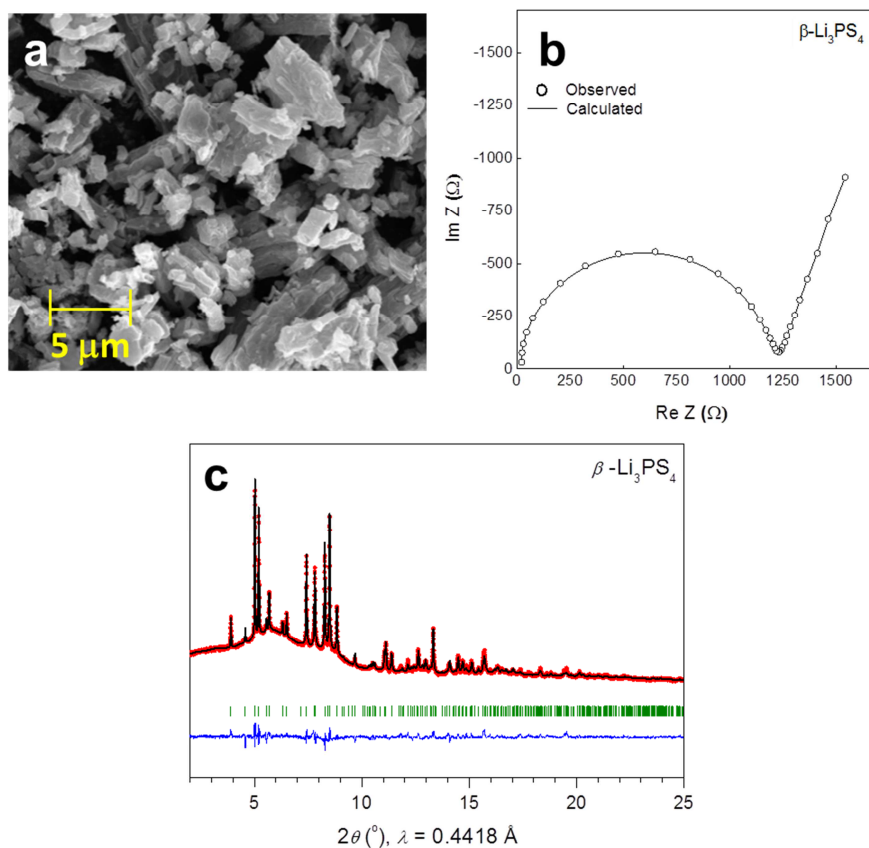


**Figure S1.**  $\beta$ - $\text{Li}_3\text{PS}_4$  solid electrolyte characterization. (a) SEM micrograph of the as-synthesized powder. (b) Conductivity determination by EIS onto a  $\beta$ - $\text{Li}_3\text{PS}_4$  pellet (8 mm diameter, 0.98 mm thick)  $\sigma_{\text{RT}} = 0.16$  mS/cm. (c) S-XRD pattern and Rietveld refinement of pristine  $\beta$ - $\text{Li}_3\text{PS}_4$ . The red circles, black continuous line, blue line, and green tick bars represent the observed, calculated, and difference patterns, and Bragg positions, respectively. The SXRD pattern was refined in  $Pnma$  space group with unit cell parameters  $a = 12.97721(27)$  Å,  $b = 8.03258(20)$  Å,  $c = 6.12629(13)$  Å, and  $V = 638.608(25)$  Å<sup>3</sup>, in agreement with the reported structural model. (Ref: Homma, K. et al.<sup>38</sup>

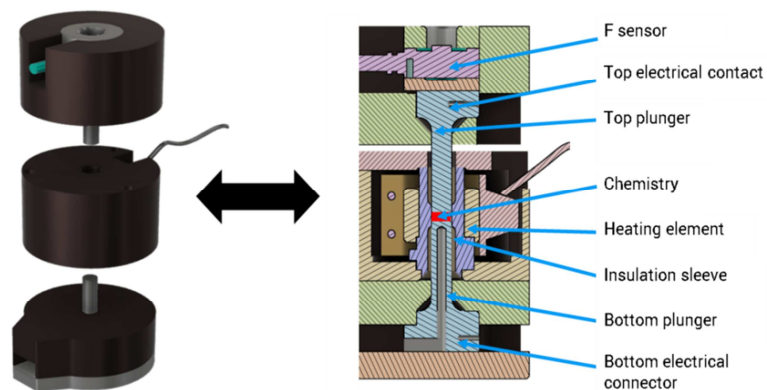


**Figure S2.** Homemate electrochemical cell for ASSB's electrochemical testing.

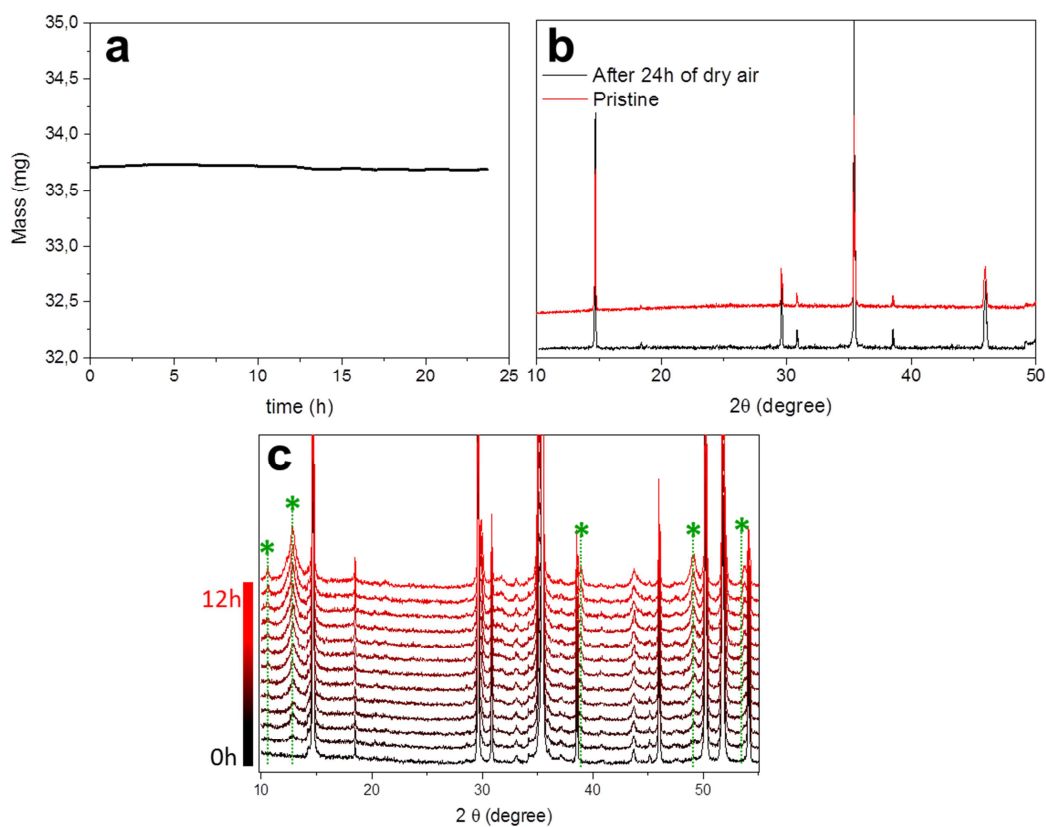


**Figure S3.** Chemical stability of pristine LTFS. (a) Isothermal TGA at 25°C and under constant flow of dry air. (b) Laboratory XRD pattern of the pristine LTFS and the LTFS sample after the

TGA experiment. (c) XRD pattern evolution of LTFS exposed to the laboratory atmosphere as a non-controlled moisture environment. The green dashed lines indicate new diffraction peaks.

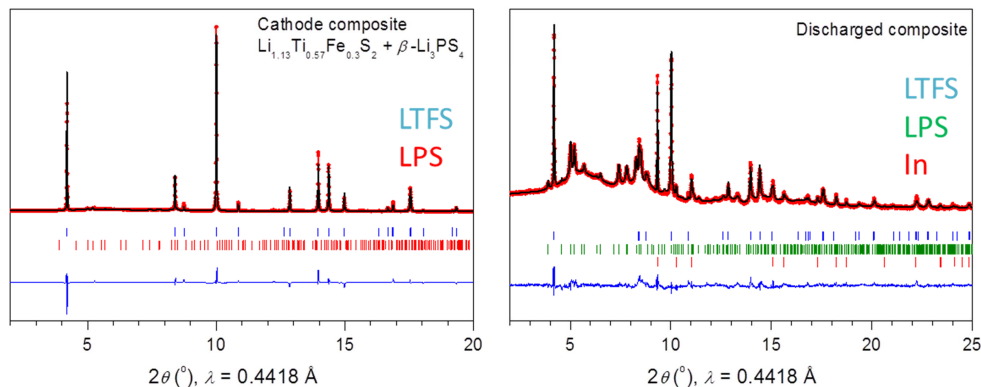


**Figure S4.** S-XRD and Rietveld refinement on LTFS/ $\beta$ - $\text{Li}_3\text{PS}_4$  (70-30 wt%) cathode composite.

(a) Pristine composite. (b) Discharged cathode composite after the first cycle of the LTFS+ $\beta$ - $\text{Li}_3\text{PS}_4$  (70-30 wt%)|| $\beta$ - $\text{Li}_3\text{PS}_4$ |InLi battery presented in [figure 2](#). Both the larger contribution of solid electrolyte and the unexpected presence of Indium have their origin in the sample preparation, as part of the electrolyte layer and traces of the anode were dragged along the scratching of the cathode side of the full battery. The red circles, black continuous line, blue line, and tick bars represent the observed, calculated, and difference patterns, and Bragg positions, respectively. In (a), the blue and red tick bars represent the Bragg positions of LTFS and  $\beta$ - $\text{Li}_3\text{PS}_4$ , respectively. For LTFS, the refinement returns  $a = b = 3.53264(2) \text{ \AA}$ ,  $c = 18.06877(16) \text{ \AA}$ , and  $V = 195.280(2) \text{ \AA}^3$ . In (c), the blue, green and red tick bars represent the Bragg positions of LTFS,  $\beta$ - $\text{Li}_3\text{PS}_4$ , and indium (In) metal. From refinement, lattice parameters  $a = b = 3.52068(5) \text{ \AA}$ ,  $c = 18.11987(33) \text{ \AA}$ , and  $V = 194.509(9) \text{ \AA}^3$  were obtained for LTFS.

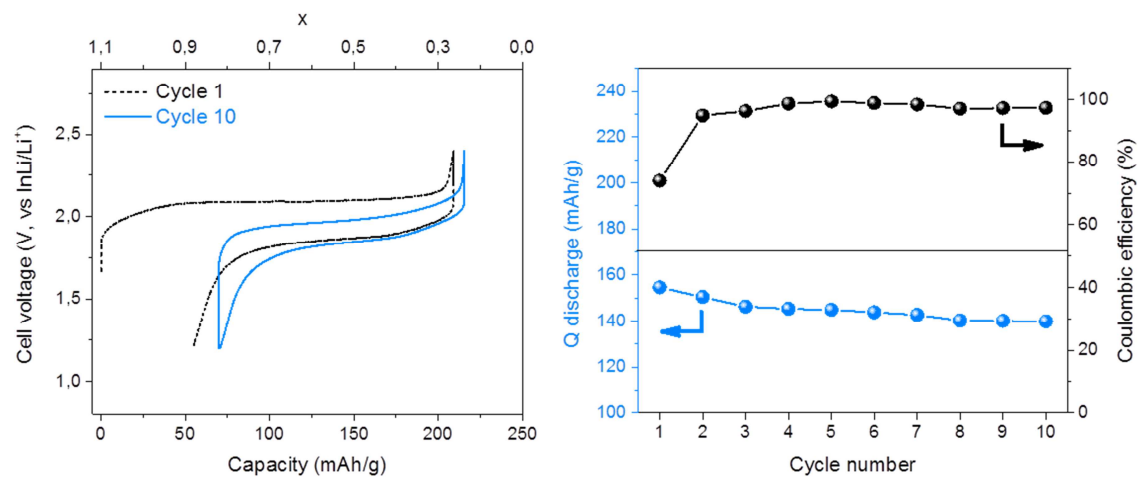


**Figure S5.** 1<sup>st</sup> and 10<sup>th</sup> galvanostatic charge/discharge cycles (LEFT), discharge capacity and coulombic efficiency (RIGHT) for the LTFS+ $\beta$ -Li<sub>3</sub>PS<sub>4</sub> (70-30 wt%)/ $\beta$ -Li<sub>3</sub>PS<sub>4</sub>/InLi battery cycled at C/50 and at room temperature.

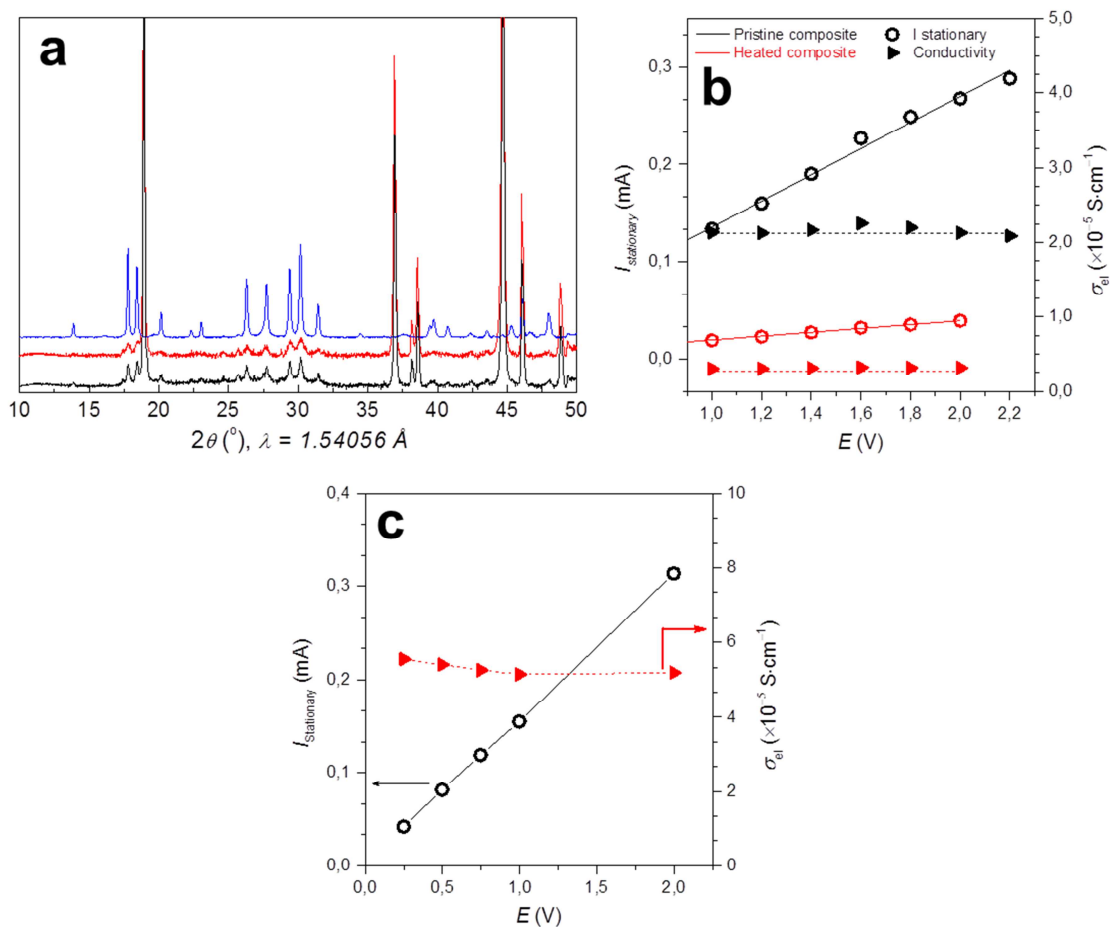


**Figure S6.** (a) Laboratory XRD patterns of pristine NMC/β-Li<sub>3</sub>PS<sub>4</sub> (70:30 wt. %) composite (black), heated NMC/β-Li<sub>3</sub>PS<sub>4</sub> (70:30 wt. %) composite at 200°C for 5 days (red) and pristine β-Li<sub>3</sub>PS<sub>4</sub> (blue). (b) DC conductivity on a pelletized pristine and heated NMC/β-Li<sub>3</sub>PS<sub>4</sub> (70:30 wt. %) composite. (c) DC conductivity on a pelletized NMC 622/LTFS/β-Li<sub>3</sub>PS<sub>4</sub> (63:7:30 wt.%) composite



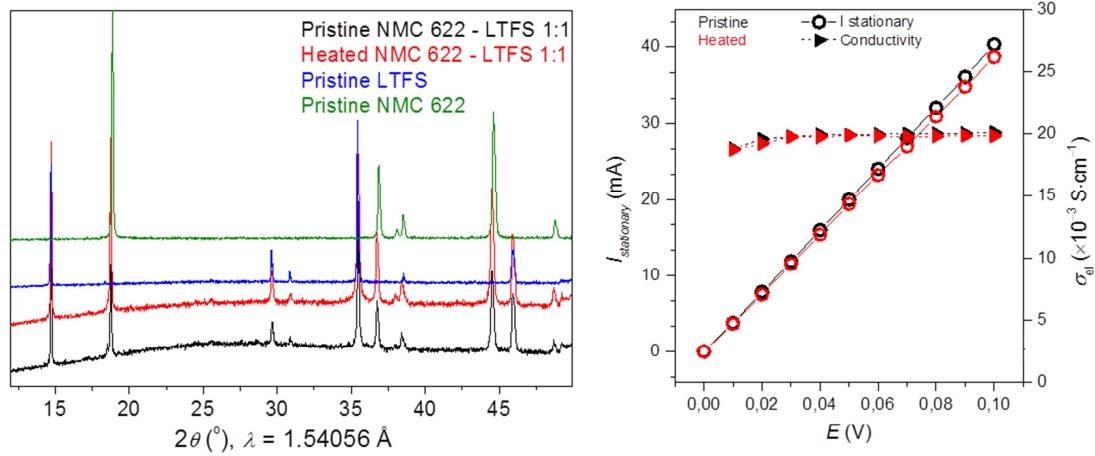


**Figure S7.** (a) Laboratory XRD patterns of pristine NMC/LTFS (1:1 wt. %) composite (black), NMC/LTFS (1:1 wt. %) composite after heating at 200°C for 5 days (red), pristine LTFS (blue) and pristine NMC 622 (green). (b) DC conductivity on a pelletized pristine and heated NMC/LTFS (1:1 wt. %) composite.

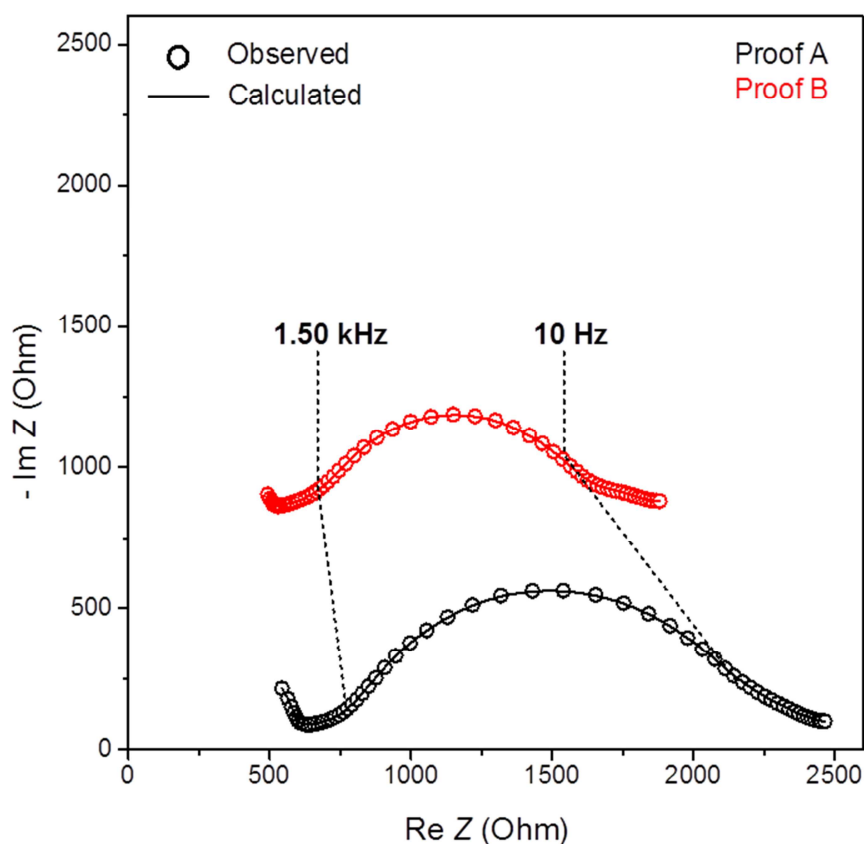


**Figure S8.** Nyquist plots from EIS measurements performed on Battery A (black) and Proof Battery B (red) after the 1<sup>st</sup> galvanostatic charge. The measurements were performed after a resting period of 20h and in a frequency range 100 kHz – 100 mHz. Experimental data was fitted with a (RQ)(RQ) equivalent circuit. The spectrum of Proof battery A was intentionally shifted - 800  $\Omega$  in the Y axis for clearer plotting.

## CORRESPONDING AUTHOR

Corresponding author : Jean Marie Tarascon\*

e-mail: jean-marie.tarascon@college-de-france.fr

## ACKNOWLEDGMENTS

The authors acknowledge to ALBA synchrotron facility for the S-XRD experiments, to Ingénieur d'études David Montero (Institut des Matériaux de Paris Centre, CNRS) for the SEM imaging and to MsC Laura Alberio Blanquer (Collège de France, Chaire de Chimie du Solide et de l'Energie) for the TGA experiments.

## REFERENCES

- (1) Tarascon, J. M.; Armand, M. Issues and Challenges Facing Rechargeable Lithium Batteries. *Nature*. November 15, 2001, pp 359–367. <https://doi.org/10.1038/35104644>.
- (2) Tarascon, J. M.; Delacourt, C.; Prakash, A. S.; Morcrette, M.; Hegde, M. S.; Wurm, C.; Masquelier, C. Various Strategies to Tune the Ionic/Electronic Properties of Electrode Materials. *Dalton Transactions*. October 7, 2004, pp 2988–2994. <https://doi.org/10.1039/b408442j>.
- (3) Lu, Z.; Dahn, J. R. Understanding the Anomalous Capacity of Li/Li[NixLi(1/3-2x/3)Mn(2/3-x/3)]O2 Cells Using in Situ X-Ray Diffraction and Electrochemical Studies. *J. Electrochem. Soc.* **2002**, *149* (7). <https://doi.org/10.1149/1.1480014>.
- (4) Janek, J.; Zeier, W. G. A Solid Future for Battery Development. *Nat. Energy* **2016**, *1* (9), 16141. <https://doi.org/10.1038/nenergy.2016.141>.
- (5) LIANG CC; EPSTEIN J; BOYLE GH. HIGH-VOLTAGE, SOLID- STATE BATTERY SYSTEM- 2. *J. Electrochem. Soc.* **1969**, *116* (10), 1452–1454. <https://doi.org/10.1149/1.2412312>.
- (6) Kamaya, N.; Homma, K.; Yamakawa, Y.; Hirayama, M.; Kanno, R.; Yonemura, M.; Kamiyama, T.; Kato, Y.; Hama, S.; Kawamoto, K.; et al. A Lithium Superionic Conductor. *Nat. Mater.* **2011**, *10* (9), 682–686. <https://doi.org/10.1038/nmat3066>.
- (7) Park, K. H.; Bai, Q.; Kim, D. H.; Oh, D. Y.; Zhu, Y.; Mo, Y.; Jung, Y. S. Design Strategies, Practical Considerations, and New Solution Processes of Sulfide Solid Electrolytes for All-Solid-State Batteries. *Adv. Energy Mater.* **2018**, *8* (18), 1–24. <https://doi.org/10.1002/aenm.201800035>.
- (8) Murayama, M.; Sonoyama, N.; Yamada, A.; Kanno, R. Material Design of New Lithium Ionic Conductor , Thio-LISICON , in the Li 2 S – P 2 S 5 System. **2004**, *170*, 173–180. <https://doi.org/10.1016/j.ssi.2004.02.025>.
- (9) Pfenninger, R.; Struzik, M.; Garbayo, I.; Stilp, E.; Rupp, J. L. M. A Low Ride on

- Processing Temperature for Fast Lithium Conduction in Garnet Solid-State Battery Films. *Nat. Energy* **2019**, 4 (6), 475–483. <https://doi.org/10.1038/s41560-019-0384-4>.
- (10) Han, F.; Yue, J.; Chen, C.; Zhao, N.; Fan, X.; Ma, Z.; Gao, T.; Wang, F.; Guo, X.; Wang, C. Interphase Engineering Enabled All-Ceramic Lithium Battery. *Joule* **2018**, 2 (3), 497–508. <https://doi.org/10.1016/j.joule.2018.02.007>.
  - (11) Wenzel, S.; Randau, S.; Leichtweiß, T.; Weber, D. A.; Sann, J.; Zeier, W. G.; Janek, J. Direct Observation of the Interfacial Instability of the Fast Ionic Conductor Li<sub>10</sub>GeP<sub>2</sub>S<sub>12</sub> at the Lithium Metal Anode. *Chem. Mater.* **2016**, 28 (7), 2400–2407. <https://doi.org/10.1021/acs.chemmater.6b00610>.
  - (12) Han, F.; Westover, A. S.; Yue, J.; Fan, X.; Wang, F.; Chi, M.; Leonard, D. N.; Dudney, N. J.; Wang, H.; Wang, C. High Electronic Conductivity as the Origin of Lithium Dendrite Formation within Solid Electrolytes. *Nat. Energy* **2019**, 4 (3), 187–196. <https://doi.org/10.1038/s41560-018-0312-z>.
  - (13) Lewis, J. A.; Tippens, J.; Cortes, F. J. Q.; McDowell, M. T. Chemo-Mechanical Challenges in Solid-State Batteries. *Trends in Chemistry*. Cell Press December 1, 2019, pp 845–857. <https://doi.org/10.1016/j.trechm.2019.06.013>.
  - (14) Zhu, Y.; He, X.; Mo, Y. Origin of Outstanding Stability in the Lithium Solid Electrolyte Materials: Insights from Thermodynamic Analyses Based on First-Principles Calculations. *ACS Appl. Mater. Interfaces* **2015**, 7 (42), 23685–23693. <https://doi.org/10.1021/acsami.5b07517>.
  - (15) Takada, K.; Aotani, N.; Iwamoto, K.; Kondo, S. Solid State Lithium Battery with Oxysulfide Glass. *Solid State Ionics* **1996**, 86–88 (PART 2), 877–882. [https://doi.org/10.1016/0167-2738\(96\)00199-3](https://doi.org/10.1016/0167-2738(96)00199-3).
  - (16) Santhosha, A. L.; Medenbach, L.; Buchheim, J. R.; Adelhelm, P. The Indium–Lithium Electrode in Solid-State Lithium-Ion Batteries: Phase Formation, Redox Potentials, and Interface Stability. *Batter. Supercaps* **2019**, 2 (6), 497–497. <https://doi.org/10.1002/batt.201900073>.
  - (17) Koerver, R.; Walther, F.; Aygün, I.; Sann, J.; Dietrich, C.; Zeier, W. G.; Janek, J. Redox-Active Cathode Interphases in Solid-State Batteries. *J. Mater. Chem. A* **2017**, 5 (43), 22750–22760. <https://doi.org/10.1039/c7ta07641j>.
  - (18) Haruyama, J.; Sodeyama, K.; Han, L.; Takada, K.; Tateyama, Y. Space – Charge Layer Effect at Interface between Oxide Cathode and Sulfide Electrolyte in All-Solid-State Lithium-Ion Battery. *Chem. Mater.* **2014**, 26, 4248–4255. <https://doi.org/10.1021/cm5016959>.
  - (19) Takada, K.; Ohta, N.; Zhang, L.; Xu, X.; Hang, B. T.; Ohnishi, T.; Osada, M.; Sasaki, T. Interfacial Phenomena in Solid-State Lithium Battery with Sulfide Solid Electrolyte. *Solid State Ionics* **2012**, 225, 594–597. <https://doi.org/10.1016/j.ssi.2012.01.009>.
  - (20) Culver, S. P.; Koerver, R.; Zeier, W. G.; Janek, J. On the Functionality of Coatings for

- Cathode Active Materials in Thiophosphate-Based All-Solid-State Batteries. *Advanced Energy Materials*. Wiley-VCH Verlag 2019. <https://doi.org/10.1002/aenm.201900626>.
- (21) Xiao, Y.; Miara, L. J.; Wang, Y.; Ceder, G. Computational Screening of Cathode Coatings for Solid-State Batteries. **2019**. <https://doi.org/10.1016/j.joule.2019.02.006>.
  - (22) Assat, G.; Tarascon, J. M. Fundamental Understanding and Practical Challenges of Anionic Redox Activity in Li-Ion Batteries. *Nat. Energy* **2018**, 3 (5), 373–386. <https://doi.org/10.1038/s41560-018-0097-0>.
  - (23) Grimaud, A.; Hong, W. T.; Shao-Horn, Y.; Tarascon, J. M. Anionic Redox Processes for Electrochemical Devices. *Nature Materials*. Nature Publishing Group January 22, 2016, pp 121–126. <https://doi.org/10.1038/nmat4551>.
  - (24) Assat, G.; Iadecola, A.; Delacourt, C.; Dedryvère, R.; Tarascon, J. M. Decoupling Cationic-Anionic Redox Processes in a Model Li-Rich Cathode via Operando X-Ray Absorption Spectroscopy. *Chem. Mater.* **2017**, 29 (22), 9714–9724. <https://doi.org/10.1021/acs.chemmater.7b03434>.
  - (25) Saha, S.; Assat, G.; Sougrati, M. T.; Foix, D.; Li, H.; Vergnet, J.; Turi, S.; Ha, Y.; Yang, W.; Cabana, J.; et al. Exploring the Bottlenecks of Anionic Redox in Li-Rich Layered Sulfides. *Nat. Energy* **2019**, 4 (11), 977–987. <https://doi.org/10.1038/s41560-019-0493-0>.
  - (26) Liu, Z.; Fu, W.; Payzant, E. A.; Yu, X.; Wu, Z.; Dudney, N. J.; Kiggans, J.; Hong, K.; Rondinone, A. J.; Liang, C. Anomalous High Ionic Conductivity of Nanoporous  $\beta$ -Li<sub>3</sub>PS<sub>4</sub>. *J. Am. Chem. Soc.* **2013**, 135 (3), 975–978. <https://doi.org/10.1021/ja3110895>.
  - (27) Li<sub>3</sub>PS<sub>4</sub> Crystal Structure: Datasheet from “PAULING FILE Multinaries Edition – 2012” in SpringerMaterials ([https://Materials.Springer.Com/Isp/Crystallographic/Docs/Sd\\_1902000](https://Materials.Springer.Com/Isp/Crystallographic/Docs/Sd_1902000)). Springer-Verlag Berlin Heidelberg & Material Phases Data System (MPDS), Switzerland & National Institute for Materials Science (NIMS), Japan.
  - (28) Deng, Z.; Wang, Z.; Chu, I. H.; Luo, J.; Ong, S. P. Elastic Properties of Alkali Superionic Conductor Electrolytes from First Principles Calculations. *J. Electrochem. Soc.* **2016**, 163 (2), A67–A74. <https://doi.org/10.1149/2.0061602jes>.
  - (29) Sakuda, A.; Hayashi, A.; Tatsumisago, M. Sulfide Solid Electrolyte with Favorable Mechanical Property for All-Solid-State Lithium Battery. *Sci. Rep.* **2013**, 3, 2–6. <https://doi.org/10.1038/srep02261>.
  - (30) Froehlich, K.; Bimashofer, G.; Fafilek, G.; Pichler, F.; Cifrain, M.; Trifonova, A. Electrochemical Investigation of Thermodynamic and Transport Phenomena in LP30 Electrolyte with Various Concentrations of Conducting Salt. In *ECS Transactions*; Electrochemical Society Inc., 2016; Vol. 73, pp 83–93. <https://doi.org/10.1149/07301.0083ecst>.
  - (31) Sakuda, A.; Hayashi, A.; Tatsumisago, M. Interfacial Observation between LiCoO<sub>2</sub> Electrode and Li<sub>2</sub>S-P<sub>2</sub>S<sub>5</sub> Solid Electrolytes of All-Solid-State Lithium Secondary

- Batteries Using Transmission Electron Microscopy. *Chem. Mater.* **2010**, *22* (3), 949–956. <https://doi.org/10.1021/cm901819c>.
- (32) Zhang, W.; Weber, D. A.; Weigand, H.; Arlt, T.; Manke, I.; Schröder, D.; Koerver, R.; Leichtweiss, T.; Hartmann, P.; Zeier, W. G.; et al. Interfacial Processes and Influence of Composite Cathode Microstructure Controlling the Performance of All-Solid-State Lithium Batteries. *ACS Appl. Mater. Interfaces* **2017**, *9* (21), 17835–17845. <https://doi.org/10.1021/acsami.7b01137>.
  - (33) Ma, J.; Chen, B.; Wang, L.; Cui, G. Progress and Prospect on Failure Mechanisms of Solid-State Lithium Batteries. *J. Power Sources* **2018**, *392* (189), 94–115. <https://doi.org/10.1016/j.jpowsour.2018.04.055>.
  - (34) Sakuda, A.; Takeuchi, T.; Okamura, K.; Kobayashi, H.; Sakaebe, H.; Tatsumi, K.; Ogumi, Z. Rock-Salt-Type Lithium Metal Sulphides as Novel Positive-Electrode Materials. *Sci. Rep.* **2014**, *4*, 2–6. <https://doi.org/10.1038/srep04883>.
  - (35) Kasemchainan, J.; Zekoll, S.; Spencer Jolly, D.; Ning, Z.; Hartley, G. O.; Marrow, J.; Bruce, P. G. Critical Stripping Current Leads to Dendrite Formation on Plating in Lithium Anode Solid Electrolyte Cells. *Nat. Mater.* **2019**, *18* (10), 1105–1111. <https://doi.org/10.1038/s41563-019-0438-9>.
  - (36) Strauss, F.; Bartsch, T.; De Biasi, L.; Kim, A. Y.; Janek, J.; Hartmann, P.; Brezesinski, T. Impact of Cathode Material Particle Size on the Capacity of Bulk-Type All-Solid-State Batteries. *ACS Energy Lett.* **2018**, *3* (4), 992–996. <https://doi.org/10.1021/acsenenergylett.8b00275>.
  - (37) Park, C.; Lee, S.; Kim, K.; Kim, M.; Choi, S.; Shin, D. Electrochemical Properties of Composite Cathode Using Bimodal Sized Electrolyte for All-Solid-State Batteries. *J. Electrochem. Soc.* **2019**, *166* (3), A5318–A5322. <https://doi.org/10.1149/2.0481903jes>.
  - (38) Homma, K.; Yonemura, M.; Kobayashi, T.; Nagao, M.; Hirayama, M.; Kanno, R. Crystal Structure and Phase Transitions of the Lithium Ionic Conductor Li<sub>3</sub>PS<sub>4</sub>. *Solid State Ionics* **2011**, *182* (1), 53–58. <https://doi.org/10.1016/j.ssi.2010.10.001>.